THE JOURNAL OF PHYSICAL CHEMISTRY B

Article

pubs.acs.org/JPCB

Characterization of Nanocellulose Using Small-Angle Neutron, X-ray, and Dynamic Light Scattering Techniques

Yimin Mao,[*,†,‡] Kai Liu,[§] Chengbo Zhan,[§] Lihong Geng,[§] Benjamin Chu,[§] and Benjamin S. Hsiao[*,§]

[†]Department of Materials Science and Engineering, University of Maryland, College Park, Maryland 20742, United States

[‡]NIST Center for Neutron Research, National Institute of Standards and Technology, Gaithersburg, Maryland 20899, United States

[§]Department of Chemistry, Stony Brook University, Stony Brook, New York 11794-3400, United States

Supporting Information

ABSTRACT: Nanocellulose extracted from wood pulps using TEMPO (2,2,6,6-tetramethylpiperidine-1-oxyl radical)-mediated oxidation and sulfuric acid hydrolysis methods was characterized by small-angle neutron scattering (SANS), small-angle X-ray scattering (SAXS), and dynamic light scattering (DLS) techniques. The dimensions of this nanocellulose (TEMPO-oxidized cellulose nanofiber (TOCN) and sulfuric acid hydrolyzed cellulose nanocrystal (SACN)) revealed by the different scattering methods were compared with those characterized by transmission electron microscopy (TEM). The SANS and SAXS data were analyzed using a parallelepiped-based form factor. The width and thickness of the nanocellulose cross section were ~8 and ~2 nm for TOCN and ~20 and ~3 nm for SACN, respectively, where the fitting results from SANS and SAXS profiles were consistent with each other. DLS was carried out under both the V_V mode with the polarizer and analyzer parallel to each other and the H_V mode having them perpendicular to each other. Using rotational and translational diffusion coefficients obtained under the H_V mode yielded a nanocellulose length qualitatively consistent with that observed by TEM, whereas the length derived by the translational diffusion coefficient under the V_V mode appeared to be overestimated.

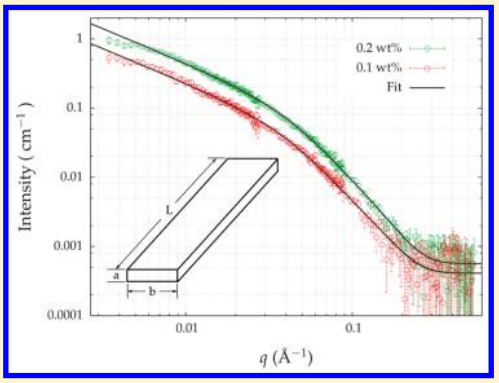

INTRODUCTION

Characterization of nanocellulose (NC), comprising a wide range of nanoscale cellulose entities, has attracted a great deal of research interest recently. These nanomaterials share a common molecular backbone (i.e., cellulose), but their morphology such as size and shape and properties such as surface charge and solution phase behavior can vary greatly depending upon the material source and the extraction method used. There are many promising applications of these nanomaterials, including nanocomposites,[1−6] water purification,[7−9,10] and clinic treatment,[11,12] whereas the potential of their usage will grow very rapidly when cheaper fabrication processes are discovered and low valued biomass sources are used.

It is known that cellulose microfibrils are the major component in plant cell walls, serving as the basic building block for providing a cell's mechanic strength. In a cell membrane, cellulose macromolecules are synthesized through cellulose synthase complexes, with the repeating unit being cellobiose (glucose dimer),[13−15] where these polymeric chains are self-assembled into microfibrils by complex molecular interactions involving hydrophobic aggregation, hydrogen bonding, geometric confinement, etc.[1,16] Cellulose microfibrils typically contain only tens of cellulose chains with a cross section in a near square shape, whereas the corresponding crystallinity is relatively low due to the large surface to volume ratio. However, microfibrils can aggregate into larger ribbon-like entities, forming cellulose nanofibers in a hierarchical manner, and they can further crystallize into cellulose nanocrystals with higher crystallinity during the extraction process.

In varying nanocellulose extraction processes, sulfuric acid hydrolysis is a common method that can produce cellulose nanocrystals. The method was first reported in the 1950s,[17,18] and has been investigated quite extensively since the 1990s.[19−21] Although several variations in processing conditions have been demonstrated, this method is generally based on the dissociation of microscale celluloses in concentrated sulfuric acid (mass fraction of ~60%) for a short period of time (e.g., an hour) at mild temperatures (e.g., ~40 °C), followed by several post-treatment steps, such as centrifugation, dialysis, and ultrasonication. This method can produce cellulose nanocrystals with a length of ~100 nm and a characteristic cross-sectional dimension of ~20 nm. Due to the sulfuric etherification reaction, hydroxyl groups on the surface of cellulose crystals are randomly replaced by sulfate ester groups, where the resulting system can form a stable colloidal suspension.

Received: November 13, 2016
Revised: January 11, 2017
Published: February 2, 2017

DOI: 10.1021/acs.jpcb.6b11425
J. Phys. Chem. B 2017, 121, 1340−1351

In the 1990s, a new method was introduced to produce finer cellulose nanofibers using the TEMPO (2,2,6,6-tetramethylpiperidine-1-oxyl radical)-mediated oxidation approach.[22−26] The TEMPO oxidation can selectively oxidize hydroxyl groups at the C6 position on the cellulose surface and create carboxylate groups, where the dispersed nanocellulose particles can also form a colloidal suspension in an aqueous environment. The resulting cellulose nanofibers usually have smaller cross-sectional dimensions (2−8 nm) and longer length. The length can vary significantly, depending on the cellulose sources and processing conditions, such as TEMPO agent concentration, reaction time, ultrasonication interval, etc. Due to the electrostatic repulsion, a stable nanocellulose suspension can be maintained for several months. In addition, the much larger aspect ratio of TEMPO-oxidized cellulose nanofiber (TOCN), as compared to that of sulfuric acid hydrolyzed cellulose nanocrystal (SACN), can enable the TOCN suspension to form a gel at much lower concentrations (typically at a mass fraction of ∼0.2%).

Due to the increasing interests in nanocellulose research, it has become necessary to find ways that can rapidly determine the dimensions of nanocellulose in the dispersion state considering the very large amount of potential samples from different biomass resources and fabrication methods one can use. The conventional microscopic techniques such as transmission electron microscopy (TEM) and scanning electron microscopy (SEM) are time-consuming and do not always reveal the desired information. This is because, for EM measurements, suitable samples must be prepared on special supports/grids. The sample preparation process always involves a drying step, in which the nanocellulose particles can aggregate into larger sizes due to the hydrophobic interactions.

The purpose of this paper is to demonstrate that varying scattering techniques can be used to determine the dimensions of nanocellulose, from nanoscale to submicroscale, in the dispersion state. In this study, small-angle neutron scattering (SANS), small-angle X-ray scattering (SAXS), and dynamic light scattering (DLS) were used to determine statistically averaged dimensions of individual nanocellulose. The results were carefully compared with those typically observed by TEM. SANS and SAXS experiments were carried out as static measurements, where the corresponding structural information was extracted via modeling of a suitable form factor of nanocellulose particles. For DLS experiments, the estimated particle size was determined by examination of hydrodynamic properties of the suspension, including translational and rotational diffusions. These three scattering methods are very different from each other in terms of experimental protocols and data interpretation. We demonstrate that all scattering techniques are useful to extract relevant dimensions of nanocellulose, providing that careful considerations of experiment procedures, data reduction, and numerical modeling in data analysis can be applied.

EXPERIMENTAL SECTION

Materials and Sample Preparation. Two types of nanocellulose, namely, TEMPO-oxidized cellulose nanofiber (TOCN) and sulfuric acid hydrolyzed cellulose nanocrystal (SACN), were chosen for this study. Details of the TEMPO-oxidation processing can be found elsewhere,[26] where the major steps taken are outlined below. A 2 g portion of dry wood pulp cellulose was first soaked in 200 mL of water overnight, into which 0.2 g of sodium bromide and 0.04 g of 2,2,6,6-tetramethylpiperidine-1-oxyl were subsequently added. The oxidation reaction was initiated by adding 30 g of sodium hypochlorite (mass fraction between 10 and 13% aqueous solution). The mixture was stirred at room temperature for 24 h, with the pH value being maintained between 10.0 and 10.3. The reaction was terminated by adding 10 mL of ethanol to the mixture. The resulting cellulose product was washed by centrifugation at a speed of 9000 rpm (1 rpm = 1/60 Hz) for 10 min three times. The oxidized cellulose slurry was then homogenized using ultrasonication (Cole Parmer, VCX-400) for 10 min, to produce a well-dispersed TOCN suspension (see Product Disclaimer).

Sulfuric acid hydrolyzed cellulose nanocrystal (SACN) was obtained from Alberta Innovates Technology Futures (see Product Disclaimer). The processing condition for fabricating SACN has been well documented,[19−21] where the typical procedure is as follows. A 90 g portion of sulfuric acid (mass fraction of 64%) was added to 10 g of wood pulp. With continuous stirring, the reaction was kept at 70 °C for 1 h. After that, 1 L of deionized water was subsequently added to quench the reaction, followed by washing and centrifugation. The resulting nanocellulose suspension was dialyzed using deionized water until the pH of the surrounding water became neutral. The suspension was then spray-dried to form the cellulose nanocrystal powder.

Small-Angle Neutron Scattering. The small-angle neutron scattering (SANS) experiment was carried out at the NG7-30m SANS beamline[27] in NIST Center for Neutron Research (NCNR), National Institute of Standards and Technology (NIST). Three instrumental configurations, with sample-to-detector distances (SDD) being 1, 4, and 13 m, respectively, were used to cover a broad q-range (q is the modulus of scattering vector; $q = (4\pi/\lambda)\sin(\theta/2)$, with λ being the neutron wavelength and θ being the scattering angle) from ∼0.003 to ∼0.5 $Å^{-1}$. A 6 Å neutron wavelength was used, and the wavelength spread was ∼13%. The transmission coefficient of the sample was determined by taking the ratio of the incident neutron beam (attenuated) intensities measured with and without the sample. 1D SANS curves were normalized to produce absolute scattering intensity.

Demountable titanium cells were used as the sample holders. Cell windows were made of quartz, and the window aperture had a diameter of 19 mm to allow the neutron beam (diameter = 12.7 mm) to pass through. The sample thickness varied: 2 mm thickness cells were used for TOCN suspension samples, and 1 mm thickness cells were used for SACN samples. The accurate thickness of all cells was calibrated by measuring the neutron transmission of cells containing only deionized water.

To increase the scattering contrast, nanocellulose were dispersed in D_2O. For TOCN, the D_2O/H_2O exchange was carried out in suspension after TEMPO oxidation, where the suspension was repeatedly centrifuged followed by washing for three times. As SACN samples were more hydrophilic due to the charged sulfate ester groups on the nanocellulose surface, dry powders were directly dispersed in D_2O. All nanocellulose suspensions were ultrasonicated for 10 min after solvent exchange, and were centrifuged at 12,000 rpm for 20 min before loading into sample cells. The scattering data from empty cell and cell filled with only D_2O were measured for background subtraction purposes.

Data reduction involving averaging 2D data into 1D curves and construction of a single SANS curve from data measured at

DOI: 10.1021/acs.jpcb.6b11425
J. Phys. Chem. B 2017, 121, 1340−1351

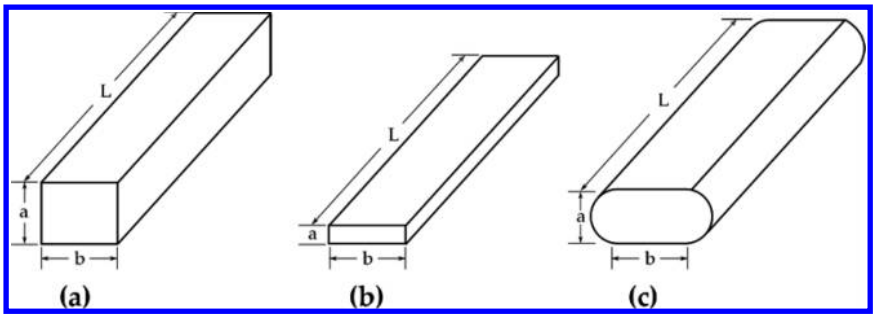

Figure 1. Schematics of extrusions with rectangular-shaped cross section: (a) parallelepiped model where thickness a and width b could take arbitrary values; (b) ribbon model where $b \gg a$; the ribbon model produced the same small-angle scattering curve as that modeled using the cross section of the rectangle with semicircle ends, shown in part c.

three different SDDs was carried out using the IGOR macro (available from NCNR) developed by S. Kline.[28]

Small-Angle X-ray Scattering. The small-angle X-ray scattering (SAXS) experiment was carried out at the beamline 7.3.3[29] in Advance Light Source (ALS), Lawrence Berkeley National Laboratory (LBNL). The chosen X-ray energy was 10 keV (λ = 1.2398 Å). The SDD was 2.789 m, which covered a q-range from ~0.006 to ~0.28 Å^{-1}. A Pilatus 2 M 2D detector was used to capture the scattering images (see Product Disclaimer). Both the beam center and SDD were calibrated using a silver behenate standard. The X-ray exposure time was 5 min for each sample.

It was critical in solution-SAXS experiments to maintain all unwanted background static and the same. A custom-built flow-cell was used as the sample holder, which ensured the correct capturing of sample and background scattering images. The chosen diameter of the capillary was 2 mm. For our aqueous suspension samples, the X-ray beam was attenuated by about 70%. Two ionic chambers were installed before and after the flow cell to determine the beam attenuation by the sample. Scattering from pure water and the empty cell was also measured to ensure correct background subtraction. Conversion of 2D data to 1D profiles was carried out using the Nika IGOR macro developed by J. Ilavsky.[30]

Dynamic Light Scattering. Dynamic light scattering (DLS) experiments were carried out using a Brookhaven BIC multiangle light scattering apparatus (see Product Disclaimer). The laser wavelength was 532 nm. Two scattering modes were used. In the first mode, the polarizer and analyzer before and after the sample were arranged in a parallel fashion (both were perpendicular to the scattering plane), denoted as the V_V mode. To investigate the rotational diffusion of anisotropic particles, the depolarized mode was also used where the polarizer was positioned perpendicular to the scattering plane but the analyzer was parallel to the scattering plane, denoted as the H_V mode. Scattering measurements were performed at multiple angles from 30 to 140°.

Suspension samples were centrifuged at 12,000 rpm for 20 min before DLS experiments. In the V_V mode, samples with four concentrations were measured, where the diffusion coefficient was obtained by concentration extrapolation, which will be described later. The typical counting time in this mode was ~10 min. However, in the H_V mode, the sample at only one concentration (mass fraction of 0.2% for TOCN and of 0.1% for SACN) was measured, as the detector count rate was significantly lower than that in the V_V mode: ~3 h was needed in the H_V measurement to produce a correlation function with acceptable statistics.

The theoretical background in DLS can be briefed as follows. In self-beating mode, DLS measures the second-order correlation function $G^{(2)}(q, \tau)$, namely, intensity−intensity correlation function. At a given q value, it is defined as[31]

$$G^{(2)}(q, \tau) = \langle I(t)I(t + \tau)\rangle \quad (1)$$

where $\langle I(t)I(t + \tau)\rangle$ is the intensity correlation function and τ is the decay time. The Sergiet relation correlates $G^{(2)}(q, \tau)$ with the first-order correlation function $g^{(1)}(q, t)$

$$G^{(2)}(q, \tau) = A(1 + \beta[g^{(1)}(q, \tau)]^2) \quad (2)$$

where A is the baseline and β is the beating efficiency depending on optics and alignment. After normalization, eq 2 can be written as

$$g^{(2)}(q, \tau) - 1 = \beta[g^{(1)}(q, \tau)]^2 \quad (3)$$

In DLS, dynamic information on particles (colloid, polymer coil, etc.) is included in $g^{(1)}(q, \tau)$, which often shows an exponential decay

$$g^{(1)}(q, \tau) = G \exp(-\Gamma\tau) \quad (4)$$

where G is simply a proportional factor and Γ represents the line-width, which is related to the particle diffusion coefficient, D. For a polydispersed system, the correlation function is a linear summation of multiple exponential decays, each corresponding to a diffusion coefficient due to the motion of particles with different sizes. Hence,

$$g^{(1)}(q, t) = \int_0^\infty G(\Gamma) \exp(-\Gamma\tau)\, d\Gamma \quad (5)$$

where $G(\Gamma)$ is related to the particle size polydispersity. $G(\Gamma)$ can be obtained by applying the Laplace inversion of eq 5, which was done by using the CONTIN program[32,33] in this study. In this case, the mean value of Γ, written as $\langle\Gamma\rangle$, can be used to calculate diffusion coefficients, which will be described later.

Transmission Electron Microscopy. Transmission electron microscopy (TEM) was used to provide direct visualization of the nanocellulose. The sample preparation procedure is as follows. TOCN and SOCN suspensions were first diluted to a mass fraction of 0.01%, sonicated for 10 min, and subsequently coated on the TEM grid. Before drying, a mass fraction of 2.0% uranyl acetate aqueous solution was deposited on the grid and was left for 30 s to stain the sample, where the excess liquid was absorbed by filter paper. The TEM measurements were performed using a FEI Bio TwinG2

DOI: 10.1021/acs.jpcb.6b11425
J. Phys. Chem. B 2017, 121, 1340−1351

microscope equipped with a CCD camera operated with an accelerating voltage of 120 kV (see Product Disclaimer).

SANS and SAXS Data Modeling. The shape and size of nanocellulose can be modeled using a rod-like particle with appropriate cross section. However, it has been found out that the subtle details in SAXS profiles for dilute TOCN suspensions could not be fitted by a simple rigid rod model with consideration of polydispersity.[34,35] Instead, the parallelepiped model with three characteristic lengths: particle length L, thickness a, and width b (see Figure 1a) appeared to be suitable. This model, having a rectangular-shaped cross section, is consistent with typical crystallographic packing of cellulose chains. Specifically, natural crystalline cellulose can exist in I_α and I_β polymorphs, possessing triclinic and monoclinic unit cells, respectively. The oblique angles in those unit cells are both close to 90°.

The scattered intensity from the form factor of the parallelepiped model can be given by eq 6,[34] which contains three characteristic lengths, a, b, and L, in double integral over polar angle (ϕ) and azimuthal angle (ψ) in the spherical coordinate. This operation is generally computationally expensive.

$$I(q) = \frac{(abL)^2}{4\pi}\int_0^{2\pi}\int_0^{\pi} \mathrm{sinc}^2 A\ \mathrm{sinc}^2 B\ \mathrm{sinc}^2 C\ \sin\phi\ \mathrm{d}\phi\ \mathrm{d}\psi$$
$$A = qa\sin\phi\cos\psi/2,\ B = qb\sin\phi\sin\psi/2,\ C = qL\cos\phi/2 \quad (6)$$

When the particle length (L) is much larger than the cross-section dimensions (a and b), two angular averaging can be decoupled,[36] and the polar-angle average of the term involving the particle length can be reduced to $2\pi/(qL)$. Consequently, eq 6 can be rewritten as

$$I(q) = \frac{(ab)^2 L}{2}\frac{1}{q}\int_{2\pi}^{0} \mathrm{sinc}^2 X\ \mathrm{sinc}^2 Y\ \mathrm{d}\psi$$
$$\text{where } X = qa\cos\psi/2,\ Y = qb\sin\psi/2 \quad (7)$$

Su et al.[34] made a further approximation that $b \gg a$ (see Figure 1b), and eq 7 could be further simplified to

$$I(q) = \frac{(ab)^2 L}{2}\frac{1}{q}\mathrm{sinc}^2(qa/2)\int_0^{2\pi} \mathrm{sinc}^2(qb\sin\phi/2)\ \mathrm{d}\psi \quad (8)$$

The integral in eq 8 can be expressed in the form of a hypergeometric function, so that the final formula becomes the expression for the so-called ribbon model ($b \gg a$), given as follows.

$$I(q) = (ab)^2 L\pi\frac{1}{q}\mathrm{sinc}^2(qa/2)\,{}_1F_2\left(\frac{1}{2};\frac{3}{2},2;-\frac{q^2b^2}{4}\right) \quad (9)$$

Equation 9 is equivalent to the solution derived by using the cross section having two ends of semicircles, as shown in Figure 1c.[34] Therefore, it deviates from the ideal parallelepiped model, when the values of a and b become close.

In this study, we used a different approach to approximate eq 7. We note that the squared sinc function can be approximated using a Gaussian function, namely, $\sin^2 x/x^2 \approx \exp(-x^2/\beta)$. In this case, eq 7 can be rewritten as follows.

$$I(q) = \pi(ab)^2 L\frac{1}{q}\exp\left[-\frac{q^2}{8\beta}(a^2+b^2)\right]\cdot I_0\left[\frac{q^2}{8\beta}(b^2-a^2)\right] \quad (10)$$

where $I_0[x]$ represents the modified Bessel function of the first kind of zeroth order. The numerical constant $\beta = 2.59$ was chosen so that the Gaussian function and the squared sinc function possess the same height and same area within $[-\pi, \pi]$. In this scenario, eq 10 is termed the Gaussian-approximated parallelepiped model (GAP).

A comparison of the scattered intensity profiles calculated using three selected models is shown in Figure 2. All three

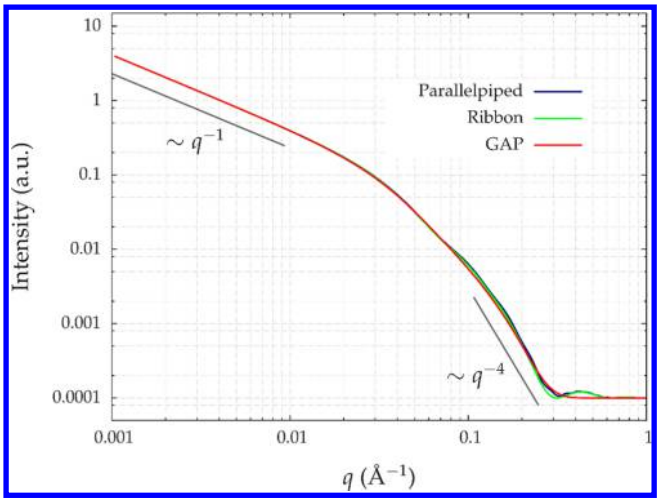

Figure 2. Comparison of scattering curves produced using the parallelepiped model, ribbon model, and Gaussian-approximated parallelepiped model (GAP). A constant baseline was added to all curves. An assumption of $L \gg a, b$ was made. The width b and thickness a of the cross section were set as 2 and 8 nm, respectively. See text for details.

models yielded similar scattered profiles. The low-q curves show an $\sim q^{-1}$ asymptote, which is due to the assumption that $L \gg a, b$. At large-q values, all profiles exhibit an $\sim q^{-4}$ asymptote, which can be explained by the presence of a sharp interface (cross section). It is seen—unlike the parallelepiped model and the ribbon model—that the scattering profile derived from the GAP model lacks the fine feature of oscillation in the large-q regime. However, notice that, in SANS/SAXS practice, one always needs to handle a finite background. Particularly at high-q regime, scattering from solution (including solvent) approaches that from pure solvent. Due to addition of variances (of data points of scattering from solution and solvent), large-q data is usually flooded by noise. In general, about 4 decades of decay in scattering intensity (after solvent background subtraction) can be observed. The GAP model behaves well within this range, and it is computationally much faster, as compared to the other two.

It is worth mentioning that, in eqs 8−10, the fiber length L appears in the prefactor; it is theoretically possible to extract length information through fitting, as absolute intensity can be measured experimentally (particularly, this is a common practice in SANS). However, this method is practically not reliable, at least for the nanocellulose system, for the following reasons. First, the scattering intensity level is concentration dependent, which can be clearly seen from Figures 3 and 5, which means an extrapolation of derived L to zero

DOI: 10.1021/acs.jpcb.6b11425
J. Phys. Chem. B 2017, 121, 1340−1351

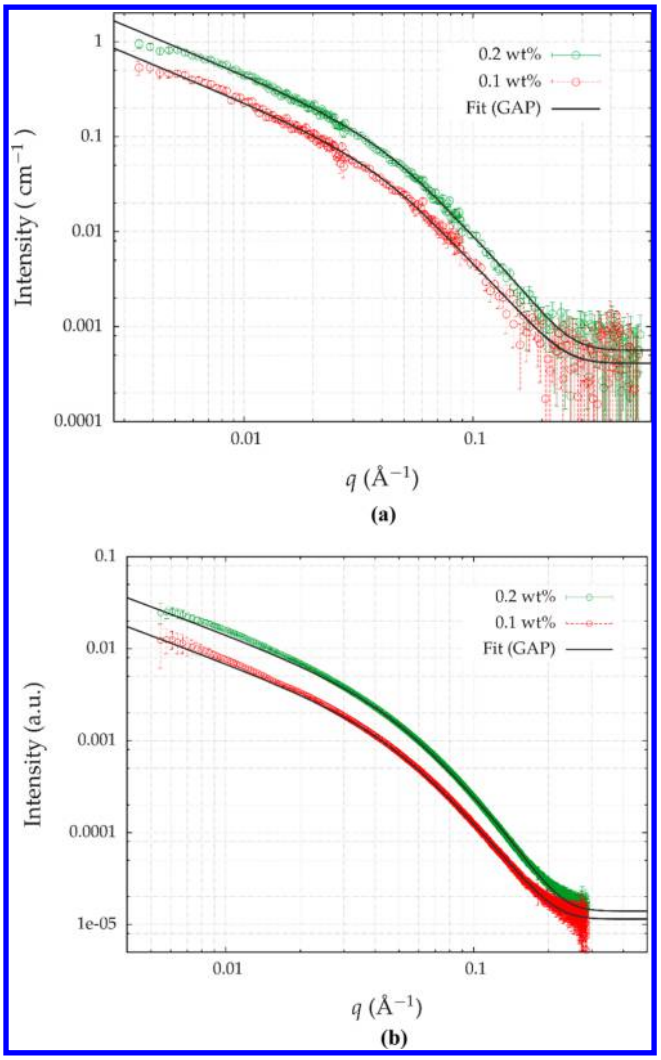

Figure 3. 1D SANS (a) and SAXS (b) curves of TOCN solutions at mass fractions of 0.1 and 0.2%. Solid lines show fitting using the GAP model. Error bars represent one standard deviation of the means (the same applies to other figures).

concentration is needed. However, it turned out the SANS/SAXS experiment for nanocellulose suspensions could only be carried out in a narrow concentration range, specifically between ~0.1 and ~0.2% (mass fraction). The lower concentration limit is determined by the scattering signal level, and the higher limit is due to overlap concentration (scales as $1/L^3$). This fact makes concentration extrapolation unreliable. Second, the scattering length density is not precisely known, as it is determined by crystallographic packing details, which is uncertain due to polymorphism and disorder (in cellulose packing). Moreover, due to the complex oxidation process, the nanocellulose surface is decorated with functional groups. Consequently, L information is "buried" in the fitting parameter of the prefactor. A feasible scattering method to determine this parameter would be to explore the Guinier regime which could appear in even lower q. This is out of the scope of the present Article.

RESULTS AND DISCUSSION

Static Measurements Using SANS and SAXS. 1D SANS and SAXS profiles of TOCN suspension samples taken at two concentrations are illustrated in Figure 3, where the fitted curves using the model are also included. Ideally, one would prepare a suspension that is sufficiently dilute, so that interparticle scattering does not play a role. However, in practice, the scattering signals can be very low with dilute suspensions. For TOCN samples, we found a mass fraction of ~0.1% was the lowest concentration limit that could still yield scattering data with acceptable statistics. As a result, only two concentrations, namely, mass fractions of 0.1 and 0.2%, were used for SANS measurement.

The fitting results using the GAP model, containing two cross-sectional dimensions, a and b, are summarized in Table 1. It is seen that both SANS and SAXS methods yielded similar results; i.e., the TOCN particles possess an average thickness of ~2 nm and average width of ~8 nm. From the biosynthesis standpoint, these results may indicate the following. As cellulose chains are synthesized from the terminal complex, they can aggregate and crystallize into elementary microfibrils, containing only a few unit cells in the cross-sectional plane. Elementary microfibrils, together with other components such as hemicelluloses, can further assemble into nanocellulose particles. The TEMPO-mediated oxidation method effectively "disintegrates" large cellulose aggregates (e.g., macrofibers), producing finer nanocellulose units. The flat shape of nanocellulose particles, as revealed by both SANS and SAXS data, suggests that the attack of TEMPO oxidant on the crystalline cellulose aggregates must have a preferred direction. This is reasonable, as cellulose chains, unlike starch molecules, possess a sheet-like configuration in the crystal form. As a result, the molecular interactions along the different crystallographic planes are expected to be different. For example, Langan et al.[37−39] have carried out the complete crystal structure determination of I_α and I_β polymorphs in cellulose crystals, using X-ray and neutron fiber diffraction methods. In their study, the hydrogen bonding networks in two crystal forms were mapped out using the deuterium replacement technique. It turned out hydrogen bonds exhibited strong directionality in both polymorphs: They were in the plane of 110 for I_α-crystal and the plane of 100 for I_β-crystal. It is conceivable that the exfoliation of nanocellulose in macroscale aggregates is associated with the dissolution of hemicellulose chains and the directionality of the hydrogen bonding plane where the attack of oxidant molecules may be the easiest.

In Figure 3, the scattering data in the low-q regime of both SANS and SAXS profiles exhibited a q^{-1} asymptote. SANS measurement could probe a slightly lower q-range; a slight intensity bend-over is observed when $q <$ ~0.005 Å^{-1}. Owing to fiber length polydispersity, it is possible that a population of

Table 1. Cross-Sectional Dimensions of TOCN Derived from SANS and SAXS Methods (Standard Deviations of Each Parameter Generated by Fitting GAP Model Were Given in Parentheses)

mass fraction	a (nm)/SANS	a (nm)/SAXS	b (nm)/SANS	b (nm)/SAXS
0.1%	1.7 (0.15)	1.7 (1.0×10^{-2})	8.2 (0.17)	7.7 (4.4×10^{-3})
0.2%	1.7 (7.8×10^{-2})	2.3 (7.3×10^{-3})	8.0 (9.1×10^{-2})	7.8 (1.3×10^{-2})

DOI: 10.1021/acs.jpcb.6b11425
J. Phys. Chem. B 2017, 121, 1340−1351

short fibers can cause scattering intensity to reach the Guinier regime at low q. However, we also need to be aware that the 13 m SDD instrumental configuration in SANS, which is responsible for low-q data, had much lower neutron flux as compared to that in 4 and 1 m SDDs. Thus, inaccuracy in solvent background subtraction near the beam stop also needs to be considered.

It is noted that the low-q data in Figure 3b deviate slightly from the model. This is due to residual aggregates in suspensions. It does not influence fitting results of cross-sectional dimensions, as they are mainly determined by intensity transition occurring in mid-q after $\sim q^{-1}$ scaling.

In Figure 4, the theoretical small-angle scattering profiles of parallelepipeds with different lengths in the q-range between

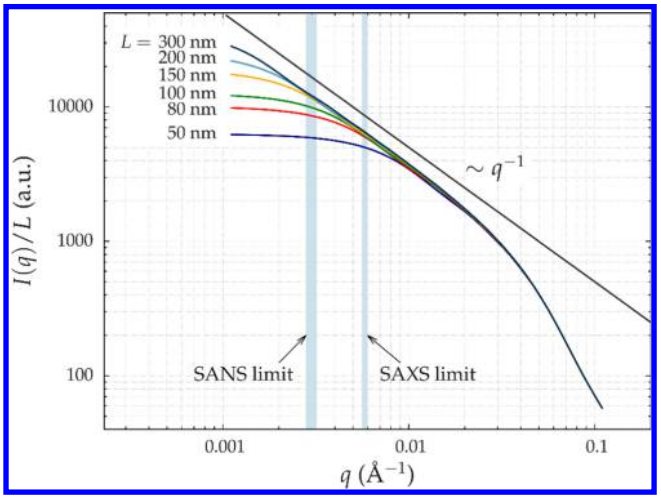

Figure 4. Calculated 1D scattering curves in the mid- to low-q regime by using the parallelepiped model with different lengths. The cross section width b and thickness a are fixed at 2 and 8 nm, respectively. Low-q detector limits in SANS and SAXS experiments are indicated in shaded areas.

0.001 and 0.1 Å^{-1}, calculated using eq 6 with the cross-section dimensions fixed at a = 2 nm and b = 8 nm, are shown. When the particle is short (for instance, L = 50 nm), the scattering profile shows a clear Guinier region at q < ~0.004 Å^{-1}. As the particle length increases, the Guinier regime moves toward a lower q value. When L > ~150 nm, the Guinier regime is less than 0.002 Å^{-1}, which cannot be observed in our SANS data. All calculated scattering profiles are consistent after the low-q regime. This indicates that, by selecting scattering data in an appropriate q-range, the structural information on particle length and cross-section dimensions can be decoupled. In our detection ranges of SANS and SAXS experiments, the length information for both TOCN and SACN (shown later) cannot be unambiguously determined. Nevertheless, we note that the lower limit of the lengths should be ~150 nm.

We need to point out that, when fitting SANS and SAXS data using different models, size polydispersity was not considered, yet the data can still be fitted satisfactorily. This does not necessarily mean that our systems are monodispersed; rather, the possible reasons are as follows. When a and b are small (in the order of a few nanometers), the effect of polydispersity is mainly manifested in the high-q regime, specifically after the q^{-1} scaling. As the scattered intensity spanned over three decades in our measurements, the slower intensity decay at the high-q region (>0.1 Å^{-1}) was partially flooded by the finite background level. In other words, in SANS measurement, we need to consider the effect of instrumental smearing, whereas, in SAXS measurement, the high-q data are truncated due to the limitation of our scattering geometry. Because of these facts, especially of the absence of slower intensity decay at large q, our fitting is not sensitive to size polydispersity.

Figure 5 shows SANS and SAXS curves of SACN samples at three concentrations. The scattering profiles were also fitted

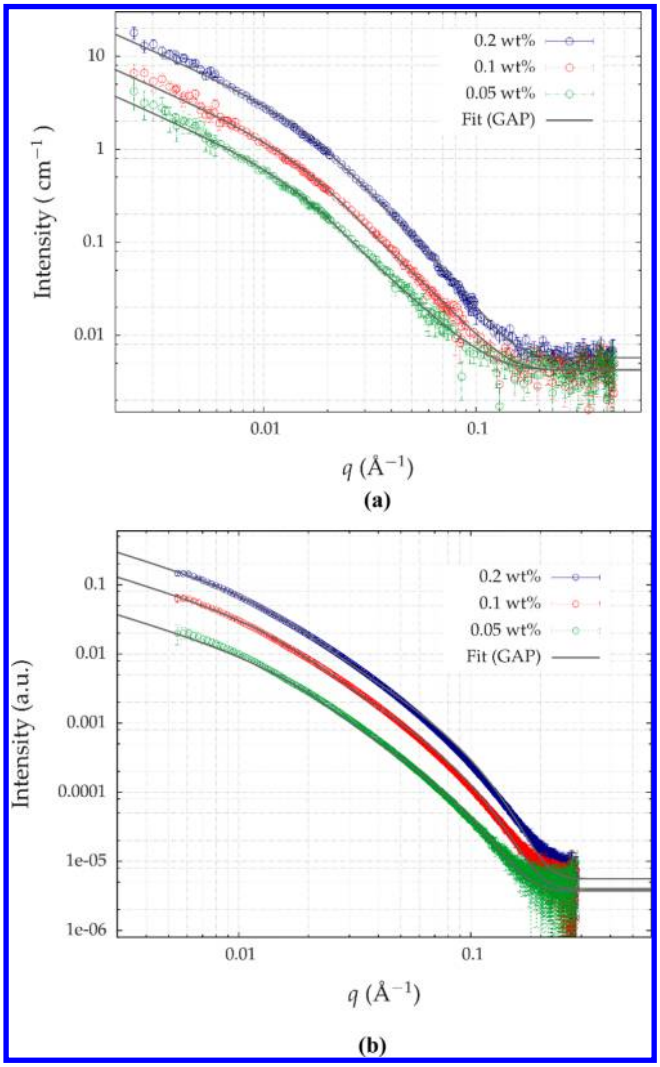

Figure 5. 1D SANS (a) and SAXS (b) curves of SACN solutions at mass fractions of 0.05, 0.1, and 0.2%. Solid lines show fitting using the GAP model.

using the GAP model, and the fitting results are shown in Table 2. As compared to TOCN samples, SACN has larger cross-section dimensions: The sizes of a and b are approximately doubled. Notice that, in parallelepiped-based models, there is a prefactor term containing $(ab)^2L$. Thus, the increase in cross-section dimension has a strong effect of increasing the scattered intensity. This was confirmed by the SANS measurement (its absolute intensity was measured), as the low-q intensity of SACN solution (Figure 5a) was about 10 times higher than that of TOCN solution (Figure 4a). The different results in the cross-section dimension of nanocellulose prepared by the different methods might be explained by the following reasons. Sulfuric acid hydrolysis is a vigorous reaction. The use of high

DOI: 10.1021/acs.jpcb.6b11425
J. Phys. Chem. B 2017, 121, 1340−1351

Table 2. Cross-Sectional Dimensions of SACN Derived from SANS and SAXS Methods (Standard Deviations of Each Parameter Generated by Fitting GAP Model Were Given in Parentheses)

mass fraction	a (nm)/SANS	a (nm)/SAXS	b (nm)/SANS	b (nm)/SAXS
0.05%	2.7 (0.18)	3.5 (0.45)	22.0 (0.37)	22.3 (0.40)
0.1%	2.7 (9.2×10^{-2})	3.1 (0.36)	20.8 (0.21)	24.0 (0.31)
0.2%	2.9 (3.9×10^{-2})	3.0 (0.31)	19.4(0.12)	24.8 (0.27)

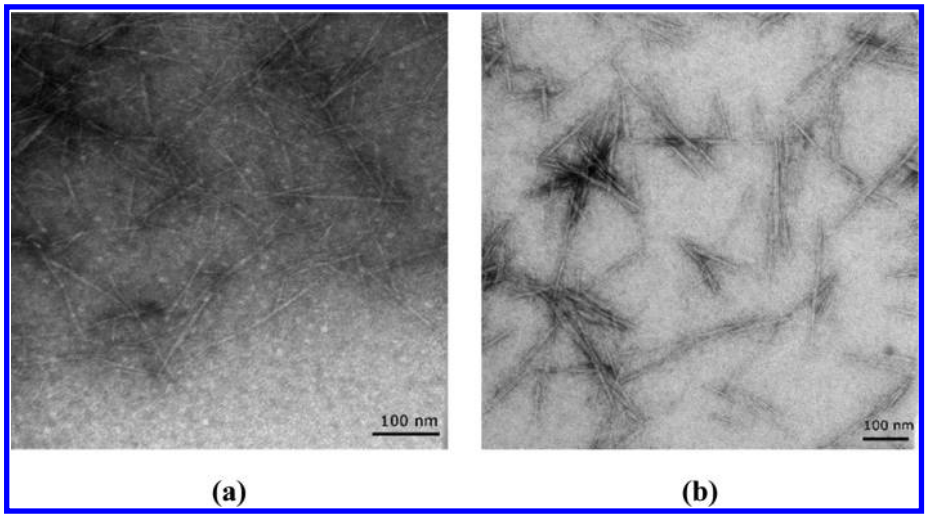

Figure 6. Transmission electron microscopic images of TOCN (a) and SACN (b).

concentration sulfuric acid (64 wt %) at an elevated temperature (45 °C) is known to be able to decompose some cellulose chains, where the process also appears to cause cellulose microfibrils to aggregate and form large cross sections. The degradation of cellulose chains (or degree of polymerization) would lead to shorter nanocrystal length, which was confirmed by the TEM measurement. In contrast, the TEMPO-mediated oxidation, taking place in a relatively mild chemical environment (pH ≈ 10), selectively converts the hydroxyl groups into the carboxylate groups at the C6 position and results in a negatively charged cellulose surface. The TEMPO-mediated oxidation process thus can enable nanocellulose particles to be gently exfoliated with less aggregation and chain degradation. As a result, the TOCN particles have smaller cross-section dimensions (and longer length due to the lesser tendency for polymer degradation) than SACN particles. Despite the difference in sizes, both SACN and TOCN samples exhibit the same characteristics of a flat cross section. This is consistent with the nature of crystallographic packing of cellulose chains.

TEM images of both TOCN and SACN samples are shown in Figure 6. Distinct size and length differences between the two nanocellulose particles are evident. However, quantitative analysis of TEM images remains difficult, as aggregates were formed during the drying process in sample preparation. Fibers in TOCN seem to be well separated (Figure 6a), while those for SACN tend to form small stacks (Figure 6b). For cross-section dimensions, present TEM images only allow probing size in one of the directions. Therefore, only qualitative agreement between results from TEM experiment and those from SANS/SAXS experiments can be reached. The average length of SACN particles was estimated, which was between 100 and 150 nm. The average length of TOCN particles was significantly longer, and the length distribution seemed to be broad (polydispersed). Because of the small cross-sectional dimensions and possible sample damage due to electron beam, the TOCN particle ends could not be definitely determined. Nevertheless, it was clear that most of them were in the order of several hundred nanometers in the view field. This observation is consistent with the notion that TEMPO-mediated oxidation is able to produce very long particles with length in the order of microns or submicrons; however, the resulting length is also dependent on the chosen cellulose species and processing conditions.

Hydrodynamic Properties Revealed by DLS. DLS is a technique that probes the quasi-elastic light scatting due to particle motion, by resolving the intensity−intensity correlation function. This method relaxes the dust-free requirement for sample preparation because micron-sized dust can be considered immobile as compared to nanoparticles that are of interest. Depending on the cellulose species and processing conditions, the length of nanocellulose particles can reach the submicron or even micron scale. For these samples, both DLS measurement and data interpretation become challenging. In our analysis, the length of SACN particles was in the range from ∼100 to ∼200 nm, and the average length of TOCN particles was shorter than ∼500 nm in general, based on the TEM measurements (Figure 6). Both suspensions were transparent, and no precipitation was observed after the centrifugation step.

A remark needs to be added in terms of carrying out DLS instead of conventional static light scattering (SLS) through, for example, Zimm-plot-type analysis. SLS has a very high requirement for a sample's "cleanliness"; even a light contamination by foreign dust present in the solution can easily ruin a measurement. This is because that SLS measures averaged intensity, and the intensity of the scattered lights scales as $\sim r^6$ (r refers to the particle diameter, assuming spherical). Therefore, it is critical to carry out a dust-freeing step before measurement, which is usually realized through

DOI: 10.1021/acs.jpcb.6b11425
J. Phys. Chem. B 2017, 121, 1340−1351

filtration. Unfortunately, this cleaning method is not applicable to dispersions containing highly asymmetric particles. Our nanocellulose suspension samples did not reach the quality as required by rigorous SLS study. DLS is feasible for not-so-clean samples due to the fact it concerns only particle dynamics, where dust particles and nanoparticles are significantly different. The scattering signal due to the unwanted event of dust entering the scattering volume can also be rejected in the data collection step through the program (of course the sample cannot be too much contaminated; this is the reason centrifugation was carried out in this study).

A relatively simple way to analyze the data from anisotropic particles is to use a thin rigid rod model, in which the decay of the first-order correlation function under the V_V and H_V modes can be written as[31,40,41]

$$g^{(1)}(q, \tau)_{VV} \propto \exp(-q^2 D_t \tau) + \gamma \exp[-(q^2 D_t + 6D_r)\tau] \quad (11a)$$

$$g^{(1)}(q, \tau)_{HV} \propto \exp[-(q^2 D_t + 6D_r)\tau] \quad (11b)$$

where D_t and D_r are the translational and rotational diffusion coefficients, respectively, and γ is a constant related to the particle anisotropy. The exponential decay of $g^{(1)}(q, t)$ can be fitted using one or multiple exponential functions, depending on the system's polydispersity. D_t and D_r can be derived by plotting the line width, $\langle\Gamma\rangle$, against q^2, and by examining the slope and the intercept. In eq 11a, at lower scattering angles, namely, $qL \ll 1$ (L is the characteristic length; in our case, the length of nanocellulose), the term in the right-hand side of the equation containing D_r vanishes, and the $g^{(1)}(q, t)_{VV}$ term becomes proportional to $\exp(-q^2 D_t t)$. In this case, D_t can be directly obtained from the slope of the $\langle\Gamma\rangle \sim q^2$ plot in the V_V mode. However, for nanocellulose particles, this means that the scattering angle should be at least less than ~30°, as their lengths usually exceed 100 nm.

In a conventional DLS device, it is typically difficult to probe the angular regime < ~30° because of the stray light due to optical alignment and defects in optical devices (such as defects in sample holders containing the index-matching fluid). The stray light can behave as a local oscillator causing heterodyne beating that will severely distort the correlation function. Due to these considerations, our DLS experiment was only carried out in the range of $30° \le \theta \le 140°$. Due to the fact that the $qL \ll 1$ requirement does not hold, the $\langle\Gamma\rangle \sim q^2$ plot in the V_V mode produces an apparent value of D_t, which can be significantly deviated from D_t determined in the H_V mode, as will be shown later. An example $\langle\Gamma\rangle \sim q^2$ plot of TOCN and SACN suspensions (mass fraction of 0.025%) under the V_V mode is shown in Figure 7 (selected autocorrelation functions and fitting results produced using CONTIN can be found in Figure S1 in the Supporting Information). Both data exhibited a linear relationship, where the apparent D_t was derived from the slope. Figure 8 shows the concentration dependence of D_t under the V_V mode. By extrapolating to zero concentration, D_t at infinitely low concentration (D_t^∞) can be obtained. They are $D_t^\infty = 3.3 \times 10^{-12}$ m^2/s and $D_t^\infty = 4.4 \times 10^{-12}$ m^2/s for TOCN and SACN particles, respectively.

DLS experiment under the H_V mode was challenging in practice because of the weak signal level. For our TOCN and SACN samples, the counting rate under the H_V mode was ~1000-fold lower than that under the V_V mode. As a result, we typically need ~3 h to produce a correlation function at one scattering angle. For this reason, measurements were only

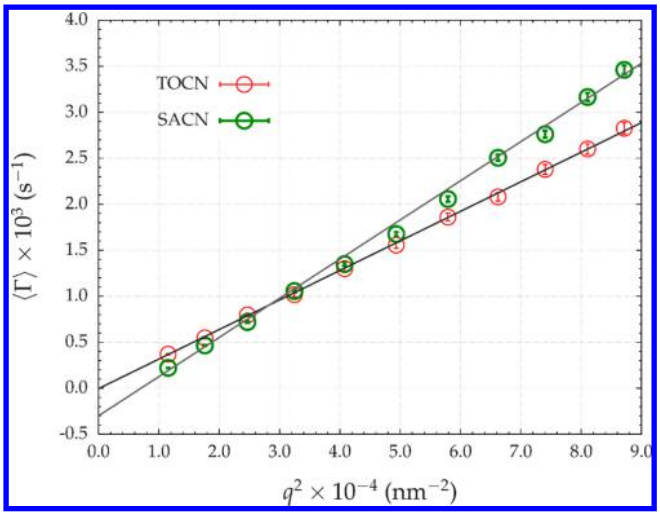

Figure 7. $\langle\Gamma\rangle \sim q^2$ plot of TOCN and SACN solutions at a mass fraction of 0.025%. Data was collected under the V_V mode of DLS.

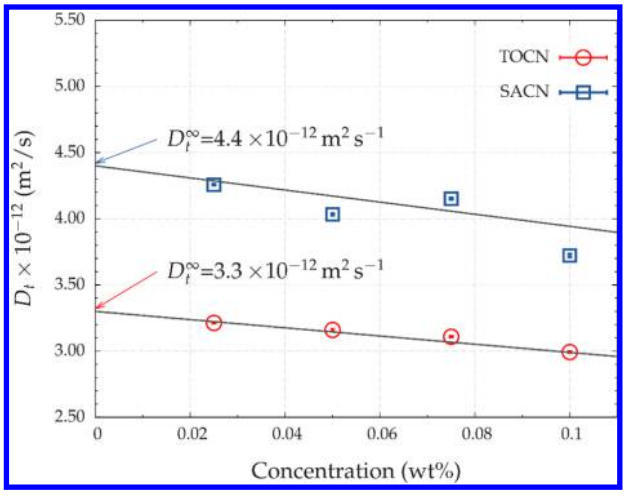

Figure 8. Translational diffusion coefficients of TOCN and SACN solutions derived under the V_V mode of DLS at different concentrations.

carried out for one concentration at six scattering angles. Figure 9 illustrates the $\langle\Gamma\rangle \sim q^2$ plot of TOCN and SACN samples. It is seen that the H_V mode data has strong angular dependence. The advantage of using the H_V mode, as indicated in eq 11b, is that D_t and D_r can be fully decoupled. The D_r values for TOCN and SACN samples are 3.0×10^3 and 4.0×10^3 s^{-1}, respectively. Compared to D_t values derived under the V_V mode, those derived from the H_V mode were ~50% higher, namely, $D_t = 4.9 \times 10^{-12}$ m^2/s for the TOCN suspension and $D_t = 6.6 \times 10^{-12}$ m^2/s for the SACN suspension (Figure 8). As discussed before, it is clear that, under the V_V mode, the apparent D_t derived from the $\langle\Gamma\rangle \sim q^2$ plot slope could be significantly influenced by the particle rotational diffusion. It will be shown later that this effect has a direct consequence, which is responsible for producing an overestimated particle length.

It is desired to correlate the diffusion coefficient to particle geometry, which can be done by adopting an appropriate hydrodynamic model. For spherical particles, the Stokes–Einstein relationship has been widely used to derive the hydrodynamic radius (denoted as r) of particles, where the diffusion coefficient is $D = k_B T/(6\pi\eta r)$; k_B is the Boltzmann

DOI: 10.1021/acs.jpcb.6b11425
J. Phys. Chem. B 2017, 121, 1340–1351

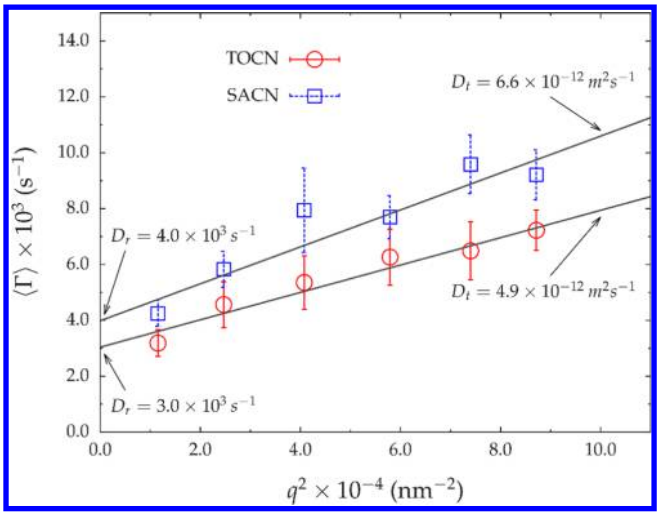

Figure 9. $\langle\Gamma\rangle \sim q^2$ plot of TOCN and SACN solutions (mass fraction of 0.2%). Data was collected under the H_V mode of DLS.

constant, T is the temperature, and η is the viscosity of the solvent.[31] For rigid rods, several diffusion modes are possible. As shown in Figure 10a and b, rods are able to translate along

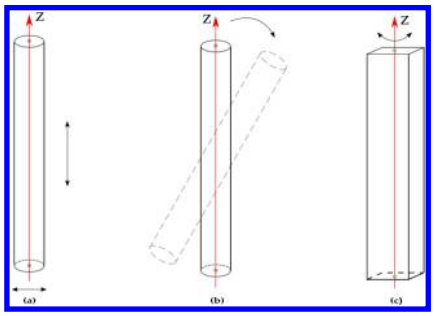

Figure 10. Illustration of different modes of motions for rod-like particles.

directions that are parallel or perpendicular to their long-axis; they are also able to rotate around axes that are perpendicular to the long-axis.

Followed the pioneering work by Kirkwood,[42,43] the hydrodynamics of a rigid rod in dilute solution has been extensively studied.[44−50] This approach was also used as a guide for our analysis. The exact analytical expression of D_t and D_r in terms of particle length L and diameter d is not available. However, with the long rod approximation, D_t and D_r can be expressed by the following forms:[50−52]

$$D_t = \frac{kT}{3\pi\eta_0 L}\ln(L/d) \tag{12a}$$

$$D_r = \frac{3kT}{\pi\eta_0 L^3}\ln(L/d) \tag{12b}$$

where p is the aspect ratio equaling L/d. As discussed earlier, both SANS and SAXS analyses revealed the rectangular-shaped cross section for nanocellulose particles. To use the hydrodynamic model for a rigid rod, we employed the radius of gyration of the rectangular cross section to approximate the rod radius. For a rectangle with the width and thickness of b and a, its radius of gyration R_g^{ab} is equal to $\sqrt{(a^2 + b^2)}/2\sqrt{3}$. Table 3 gives the lengths of TOCN and SACN calculated using eq 12. The cross-section dimensions derived from the SANS and SAXS analysis (values at different concentrations were averaged) were used for calculation. If we directly use D_t obtained under the V_V mode, the corresponding lengths for TOCN and SACN are 755.4 and 375.0 nm, respectively. These values are much larger than those observed in the TEM images. One of the major reasons for this overestimation is due to the particle anisotropy, causing the correlation function being influenced by the rotational diffusion at large angles. For long particles (length exceeding ~100 nm), the data collection in the q-range that can satisfy the $qL < 1$ criterion becomes challenging in conventional DLS devices. $2R_g^{ab}$ of a rectangle is an approximation for its "effective diameter"; the hydrodynamic model for rectangle-shaped extrusion is quite complex; and it is uncertain if it can bring new insights for a nonideal system such as a nanocellulose suspension. In Figure S2 (in the Supporting Information), L values are computed using different d ranging from 1 to 25 nm; this is done by solving eq 12 numerically. The variation of fiber length with its diameter can be looked up.

After decoupling the contributions from rotational and translational diffusions, using the D_t values under the H_V mode, the resulting particle lengths for TOCN and SACN became 458.8 and 205.1 nm, respectively. The calculated particle length dropped by ~40%, as compared to the values derived under the V_V mode. Lengths calculated by using D_r derived under the H_V mode are 174.6 and 137.6 nm for TOCN and SACN, respectively. Combined with TEM data, we believe the particle lengths derived under the H_V mode data were closer to the real condition. However, there was still a significant difference between the values derived using D_t and those using D_r. The discrepancy might stem from several sources, due to the nature of our suspension sample and the validity of the adopted hydrodynamic model which are elaborated as follows.

Table 3. Lengths of TOCN and SACN Derived Using Translational and Rotational Diffusion Coefficients, Based on the Kirkwood Model[a]

	TOCN ($2R_g^{ab}$ = 4.7 nm)			SACN ($2R_g^{ab}$ = 13.0 nm)		
diffusion mode	D_t ($m^2\ s^{-1}$) or D_r (s^{-1})	L (nm)	d_H (nm)	D_t ($m^2\ s^{-1}$) or D_r (s^{-1})	L (nm)	d_H (nm)
V_V, translation	3.3×10^{-12}	755.4	148.7	4.4×10^{-12}	375.0	111.5
H_V, translation	4.9×10^{-12}	458.8	100.2	6.6×10^{-12}	205.1	74.4
H_V, rotation	3.0×10^{3}	174.6		4.0×10^{3}	137.6	

[a]The rod diameter was approximated by $2R_g^{ab}$, where R_g^{ab} is the radius of gyration of a rectangle of thickness a and width b. Averaged a and b values derived from SANS and SAXS were used for qualitative analysis purposes. $d_H = 2r$, where r is the hydrodynamic radius derived using the Stokes−Einstein relationship. See text for details.

DOI: 10.1021/acs.jpcb.6b11425
J. Phys. Chem. B 2017, 121, 1340−1351

First of all, the Kirkwood model (in fact, most hydrodynamic models) does not consider the polydispersity in particle dimensions, which certainly adds complexity to our nanocellulose suspensions. Also, as indicated by our SANS/SAXS experiment, nanocellulose particles possess a rectangular-shaped cross section. This indicates that the rotational diffusion around the particle long axis might start to play a role in line-broadening in quasi-elastic scattering (Figure 10c). Moreover, an important factor can arise from interparticle interaction. For rod-like particles, the overlap concentration scales with $\sim 1/L^3$, which is usually much lower as compared to flexible polymers. Hindrance in particle motion in nondilute solution tends to cause diffusion coefficients being underestimated. The diffusion behavior in the semidilute regime is very different from that in the dilute regime, mainly because of the restricted particle motion and translation−rotation coupling. Furthermore, other factors associated with our TOCN and SACN samples, such as the existence of aggregates, particle flexibility (especially important for long particles), and surface charge, can all complicate the correlation between particle dimensions and hydrodynamic properties.[53]

Therefore, though DLS is sensitive to rod-like particles, the complexity of nanocellulose particles in suspension makes it challenging to be utilized as a robust measure for quantitative determination of particle sizes. We also want to point out that, by directly applying the Stokes−Einstein relationship to the translational diffusion coefficient derived under the V_V mode, a characteristic length, d_H (hydrodynamic diamteter for a spherical particle), can be obtained. These values are also listed in Table 3. d_H can be interpreted as the diameter of a spherical space a rod-like particle can effectively occupy. Using this value tends to produce an even more underestimated physical particle length. However, interestingly, d_H values in Table 3 are fairly close to those derived from rotational diffusion coefficients. Thus, DLS can serve as a convenient check of the length of a rod-like particle.

CONCLUSIONS

Nanocellulose particles prepared by TEMPO-mediated oxidation and sulfuric acid hydrolysis methods were characterized using different scattering (neutron, X-ray, and light) and microscopy techniques. The SANS and SAXS measurements were able to produce consistent information about the cross-section dimensions of the particles. Specifically, SANS and SAXS data could be modeled using the rigid parallelepiped form factor, with the assumption that the fiber length was much larger than characteristic lengths of cross section. The thickness and width of the particle cross section were ∼2 and ∼8 nm for TOCN and ∼3 and ∼20 nm for SACN. The low-resolution small-angle scattering results were consistent with the packing of natural cellulose chains in crystals, as reported in existing crystallographic studies.

DLS experiments, under both H_V and V_V modes, revealed that TOCN had larger diffusion coefficients than SACN. The Kirkwood model was used to correlate the hydrodynamic properties to the length dimensions; however, achieving quantitative characterization was challenging. The translational diffusion coefficient D_t derived under the V_V mode overestimated the lengths of the nanocellulose particles considerably, as the correlation function under the V_V mode was severely influenced by the rotational diffusion at large angles. Carrying out the DLS experiment under the H_V mode was able to decouple rotational and translational diffusion modes. The derived particle lengths were closer to the results revealed by TEM studies. There was still a significant difference between the lengths derived using the rotational diffusion coefficient and those using the translational diffusion coefficient. The reason might be due to the complexity of the systems, where the size polydispersity, rectangular-shaped cross section, solution concentration, and particle surface charge could all cause deviation from the hydrodynamic model.

ASSOCIATED CONTENT

Supporting Information

The Supporting Information is available free of charge on the ACS Publications website at DOI: 10.1021/acs.jpcb.6b11425.

Selected autocorrelation functions in the DLS experiment and their CONTIN fits (Figure S1), along with the numerical relationship of fiber diameter d and length L, computed using the rigid rod hydrodynamic model (Figure S2) (PDF)

AUTHOR INFORMATION

Corresponding Authors

*E-mail: yimin.mao@nist.gov. Phone: +13019756017.

*E-mail: benjamin.hsiao@stonybrook.edu. Phone: +16316327793.

ORCID

Yimin Mao: 0000-0002-6240-3791

Notes

Product Disclaimer: The identification of any commercial product or trade name does not imply endorsement or recommendation by the National Institute of Standards and Technology.

The authors declare no competing financial interest.

ACKNOWLEDGMENTS

The authors acknowledge the financial support of the National Science Foundation through the SusChEM program (DMR-1409507). The authors also thank the National Institute of Standards and Technology (NIST), U.S. Department of Commerce, for providing the neutron research facilities used in this work. We also want to thank Beamline 7.3.3 of the Advanced Light Source (supported by the Director of the Office of Science, Office of Basic Energy Sciences, of the U.S. Department of Energy under Contract No. DE-AC02-05CH11231) for providing the small-angle X-ray facility. Y.M. thanks Dr. Vivek M. Prabhu in the Material Measurement Laboratory (MML) division at NIST for providing the light scattering device.

REFERENCES

(1) Habibi, Y.; Lucia, L. A.; Rojas, O. J. Cellulose Nanocrystals: Chemistry, Self-Assembly, and Applications. *Chem. Rev.* **2010**, *110*, 3479−3500.

(2) Abdul Khalil, H. P. S.; Bhat, A.; Ireana Yusra, A. F. Green Composites from Sustainable Cellulose Nanofibrils: A Review. *Carbohydr. Polym.* **2012**, *87*, 963−979.

(3) Miao, C.; Hamad, W. Y. Cellulose Reinforced Polymer Composites and Nanocomposites: A Critical Review. *Cellulose* **2013**, *20*, 2221−2262.

(4) Mariano, M.; El Kissi, N.; Dufresne, A. Cellulose Nanocrystals and Related Nanocomposites: Review of Some Properties and Challenges. *J. Polym. Sci., Part B: Polym. Phys.* **2014**, *52*, 791−806.

(5) Kargarzadeh, H.; Sheltami, R. M.; Ahmad, I.; Abdullah, I.; Dufresne, A. Cellulose Nanocrystal: A Promising Toughening Agent

for Unsaturated Polyester Nanocomposite. *Polymer* **2015**, *56*, 346−357.
(6) Ching, Y. C.; Ali, M. E.; Abdullah, L. C.; Choo, K. W.; Kuan, Y. C.; Julaihi, S. J.; Chuah, C. H.; Liou, N.-S. Rheological Properties of Cellulose Nanocrystal-Embedded Polymer Composites: A Review. *Cellulose* **2016**, *23*, 1011−1030.
(7) Ma, H.; Hsiao, B. S.; Chu, B. Thin-Film Nanofibrous Composite Membranes Containing Cellulose or Chitin Barrier Layers Fabricated by Ionic Liquids. *Polymer* **2011**, *52*, 2594−2599.
(8) Ma, H.; Hsiao, B. S.; Chu, B. Ultrafine Cellulose Nanofibers as Efficient Adsorbents for Removal of UO_2^{2+} in Water. *ACS Macro Lett.* **2012**, *1*, 213−216.
(9) Ma, H.; Burger, C.; Hsiao, B. S.; Chu, B. Nanofibrous Microfiltration Membrane Based on Cellulose Nanowhiskers. *Biomacromolecules* **2012**, *13*, 180−186.
(10) Ma, H.; Burger, C.; Hsiao, B. S.; Chu, B. Ultra-Fine Cellulose Nanofibers: New Nano-Scale Materials for Water Purification. *J. Mater. Chem.* **2011**, *21*, 7507−7510.
(11) Domingues, R. M.; Gomes, M. E.; Reis, R. L. The Potential of Cellulose Nanocrystals in Tissue Engineering Strategies. *Biomacromolecules* **2014**, *15*, 2327−2346.
(12) Zhou, C.; Chu, R.; Wu, R.; Wu, Q. Electrospun Polyethylene Oxide/cellulose Nanocrystal Composite Nanofibrous Mats with Homogeneous and Heterogeneous Microstructures. *Biomacromolecules* **2011**, *12*, 2617−2625.
(13) Delmer, D. P. Cellulose Biosynthesis: Exciting Times for a Difficult Field of Study. *Annu. Rev. Plant Physiol. Plant Mol. Biol.* **1999**, *50*, 245−276.
(14) Vandavasi, V. G.; Putnam, D. K.; Zhang, Q.; Petridis, L.; Heller, W. T.; Nixon, B. T.; Haigler, C. H.; Kalluri, U.; Coates, L.; Langan, P.; et al. A Structural Study of CESA1 Catalytic Domain of Arabidopsis Cellulose Synthesis Complex: Evidence for CESA Trimers. *Plant Physiol.* **2016**, *170*, 123−135.
(15) Saxena, I. M.; Brown, R. M. Cellulose Biosynthesis: Current Views and Evolving Concepts. *Ann. Bot.* **2005**, *96*, 9−21.
(16) Fratzl, P. Cellulose and Collagen: From Fibres to Tissues. *Curr. Opin. Colloid Interface Sci.* **2003**, *8*, 32−39.
(17) Ranby, B. G. Aqueous Colloidal Solutions of Cellulose Micelles. *Acta Chem. Scand.* **1949**, *3*, 649−650.
(18) Ranby, B. G. Fibrous Macromolecular Systems. Cellulose and Muscle. The Colloidal Properties of Cellulose Micelles. *Discuss. Faraday Soc.* **1951**, *11*, 158−164.
(19) Dong, X. M.; Kimura, T.; Revol, J.-F.; Gray, D. G. Effects of Ionic Strength on the Isotropic-Chiral Nematic Phase Transition of Suspensions of Cellulose Crystallites. *Langmuir* **1996**, *12*, 2076−2082.
(20) Dong, X. M.; Gray, D. G. Effect of Counterions on Ordered Phase Formation in Suspensions of Charged Rodlike Cellulose Crystallites. *Langmuir* **1997**, *13*, 2404−2409.
(21) Dong, X. M.; Revol, J.-F.; Gray, D. G. Effect of Microcrystallite Preparation Conditions on the Formation of Colloid Crystals of Cellulose. *Cellulose* **1998**, *5*, 19−32.
(22) De Nooy, A.; Besemer, A.; Van Bekkum, H. Highly Selective TEMPO Mediated Oxidation of Primary Alcohol Groups in Polysaccharides. *Recl. Trav. Chim. Pays-Bas* **1994**, *113*, 165−166.
(23) Saito, T.; Nishiyama, Y.; Putaux, J.-L.; Vignon, M.; Isogai, A. Homogeneous Suspensions of Individualized Microfibrils from TEMPO-Catalyzed Oxidation of Native Cellulose. *Biomacromolecules* **2006**, *7*, 1687−1691.
(24) Saito, T.; Kimura, S.; Nishiyama, Y.; Isogai, A. Cellulose Nanofibers Prepared by TEMPO-Mediated Oxidation of Native Cellulose. *Biomacromolecules* **2007**, *8*, 2485−2491.
(25) Saito, T.; Hirota, M.; Tamura, N.; Kimura, S.; Fukuzumi, H.; Heux, L.; Isogai, A. Individualization of Nano-Sized Plant Cellulose Fibrils by Direct Surface Carboxylation Using TEMPO Catalyst under Neutral Conditions. *Biomacromolecules* **2009**, *10*, 1992−1996.
(26) Isogai, A.; Saito, T.; Fukuzumi, H. TEMPO-Oxidized Cellulose Nanofibers. *Nanoscale* **2011**, *3*, 71−85.
(27) Glinka, C.; Barker, J.; Hammouda, B.; Krueger, S.; Moyer, J.; Orts, W. The 30 M Small-Angle Neutron Scattering Instruments at the National Institute of Standards and Technology. *J. Appl. Crystallogr.* **1998**, *31*, 430−445.
(28) Kline, S. R. Reduction and Analysis of SANS and USANS Data Using IGOR Pro. *J. Appl. Crystallogr.* **2006**, *39*, 895−900.
(29) Hexemer, A.; Bras, W.; Glossinger, J.; Schaible, E.; Gann, E.; Kirian, R.; MacDowell, A.; Church, M.; Rude, B.; Padmore, H. A SAXS/WAXS/GISAXS Beamline with Multilayer Monochromator. *J. Phys.: Conf. Ser.* **2010**, *247*, 012007−012017.
(30) Ilavsky, J. Nika: Software for Two-Dimensional Data Reduction. *J. Appl. Crystallogr.* **2012**, *45*, 324−328.
(31) Berne, B. J.; Pecora, R. *Dynamic Light Scattering: With Applications to Chemistry, Biology, and Physics*; Courier Corporation: Mineola, New York, 1976.
(32) Provencher, S. W. A Constrained Regularization Method for Inverting Data Represented by Linear Algebraic or Integral Equations. *Comput. Phys. Commun.* **1982**, *27*, 213−227.
(33) Provencher, S. W. CONTIN: A General Purpose Constrained Regularization Program for Inverting Noisy Linear Algebraic and Integral Equations. *Comput. Phys. Commun.* **1982**, *27*, 229−242.
(34) Su, Y.; Burger, C.; Hsiao, B. S.; Chu, B. Characterization of TEMPO-Oxidized Cellulose Nanofibers in Aqueous Suspension by Small-Angle X-Ray Scattering. *J. Appl. Crystallogr.* **2014**, *47*, 788−798.
(35) Su, Y.; Burger, C.; Ma, H.; Chu, B.; Hsiao, B. S. Exploring the Nature of Cellulose Microfibrils. *Biomacromolecules* **2015**, *16*, 1201−1209.
(36) Glatter, O.; Kratky, O. *Small Angle X-Ray Scattering*; Academic Press: London, 1982.
(37) Nishiyama, Y.; Langan, P.; Chanzy, H. Crystal Structure and Hydrogen-Bonding System in Cellulose I_β from Synchrotron X-Ray and Neutron Fiber Diffraction. *J. Am. Chem. Soc.* **2002**, *124*, 9074−9082.
(38) Nishiyama, Y.; Sugiyama, J.; Chanzy, H.; Langan, P. Crystal Structure and Hydrogen Bonding System in Cellulose $I\alpha$ from Synchrotron X-Ray and Neutron Fiber Diffraction. *J. Am. Chem. Soc.* **2003**, *125*, 14300−14306.
(39) Nishiyama, Y.; Johnson, G. P.; French, A. D.; Forsyth, V. T.; Langan, P. Neutron Crystallography, Molecular Dynamics, and Quantum Mechanics Studies of the Nature of Hydrogen Bonding in Cellulose I_β. *Biomacromolecules* **2008**, *9*, 3133−3140.
(40) Chu, B. In *Soft-Matter Characterization*; Borsali, R., Pecora, R., Eds.; Springer Science & Business Media: Netherlands, 2008; pp 335−372.
(41) Zero, K.; Pecora, R. In *Dynamic Light Scattering: Applications of Photon Correlation Spectroscopy*; Pecora, R., Ed.; Plenum Press: New York, 1985; pp 59−83.
(42) Riseman, J.; Kirkwood, J. G. The Intrinsic Viscosity, Translational and Rotatory Diffusion Constants of Rod-Like Macromolecules in Solution. *J. Chem. Phys.* **1950**, *18*, 512−516.
(43) Kirkwood, J. G.; Auer, P. L. The Visco-Elastic Properties of Solutions of Rod-Like Macromolecules. *J. Chem. Phys.* **1951**, *19*, 281−283.
(44) Broersma, S. Viscous Force Constant for a Closed Cylinder. *J. Chem. Phys.* **1960**, *32*, 1632−1635.
(45) Broersma, S. Viscous Force and Torque Constants for a Cylinder. *J. Chem. Phys.* **1981**, *74*, 6989−6990.
(46) Yamakawa, H. Viscoelastic Properties of Straight Cylindrical Macromolecules in Dilute Solution. *Macromolecules* **1975**, *8*, 339−342.
(47) Yoshizaki, T.; Yamakawa, H. Dynamics of Spheroid-Cylindrical Molecules in Dilute Solution. *J. Chem. Phys.* **1980**, *72*, 57−69.
(48) Tirado, M. M.; de la Torre, J. G. Translational Friction Coefficients of Rigid, Symmetric Top Macromolecules. Application to Circular Cylinders. *J. Chem. Phys.* **1979**, *71*, 2581−2587.
(49) Tirado, M. M.; de la Torre, J. G. Rotational Dynamics of Rigid, Symmetric Top Macromolecules. Application to Circular Cylinders. *J. Chem. Phys.* **1980**, *73*, 1986−1993.
(50) de la Torre, J. G.; Bloomfield, V. A. Hydrodynamic Properties of Complex, Rigid, Biological Macromolecules: Theory and Applications. *Q. Rev. Biophys.* **1981**, *14*, 81−139.

DOI: 10.1021/acs.jpcb.6b11425
J. Phys. Chem. B 2017, 121, 1340−1351

(51) Ortega, A.; de la Torre, J. G. Hydrodynamic Properties of Rodlike and Disklike Particles in Dilute Solution. *J. Chem. Phys.* **2003**, *119*, 9914−9919.
(52) van der Zande, B. M.; Dhont, J. K.; Böhmer, M. R.; Philipse, A. P. Colloidal Dispersions of Gold Rods Characterized by Dynamic Light Scattering and Electrophoresis. *Langmuir* **2000**, *16*, 459−464.
(53) Doi, M.; Edwards, S. F. *The Theory of Polymer Dynamics*; Oxford University Press: Oxford, 1988.

DOI: 10.1021/acs.jpcb.6b11425
J. Phys. Chem. B 2017, 121, 1340−1351